Article:
Sardar, S, Kale, G orcid.org/0000-0002-3021-5905 and Ghadiri, M orcid.org/0000-0003-0479-2845 (2021) Microstructure and impedance spectroscopy of high density holmium hafnate (Ho2Hf2O7) from nanoparticulate compacts. Materials Science and Engineering: B, 265. 114989. ISSN 0921-5107

https://doi.org/10.1016/j.mseb.2020.114989

Microstructure and Impedance Spectroscopy of High Density Holmium Hafnate ($Ho_2Hf_2O_7$) from Nanoparticulate Compacts

Suneela Sardar, Girish Kale*, Mojtaba Ghadiri

School of Chemical and Process Engineering, University of Leeds, Leeds LS2 9JT, U.K.

*Corresponding Author: g.m.kale@leeds.ac.uk

Abstract

Nanoparticles of holmium hafnate ($Ho_2Hf_2O_7$) synthesised employing an environmentally sustainable Leeds Alginate Process (LAP) were compacted into pellets and sintered using conventional single step sintering (SSS) technique for 2 h over the temperature range 1100 °C to 1500 °C with the interval of 100 °C and with unconventional two-step sintering (TSS) technique at (I) -1500 °C for 5 min followed by (II) – 1300 °C for 96 h. The relative density of the pellets after sintering was calculated using the Archimedes' principle and crystal structure data was used to determine the theoretical density. Grain size was measured using ImageJ from SEM micrographs. The pellets processed by the TSS process have been found to be denser (98 %) with lesser grain growth (0.77 μm) in comparison to those processed using the SSS process. Ionic conductivities of $Ho_2Hf_2O_7$ pellets sintered by the two techniques were measured using ac-impedance spectroscopy over the temperature range of 340 °C to 750 °C using the frequency range of 100 mHz to 100 MHz for both heating and cooling cycles. The bulk (1.0×10^{-4} $S.cm^{-1}$) and grain boundary (4.66×10^{-5} $S.cm^{-1}$) conductivities of $Ho_2Hf_2O_7$ at 700 °C prepared by SSS process is slightly higher than those processed by TSS process. The value of grain boundary activation energy is lower in the case of TSS process than that of SSS process. The results of this study indicates that the ionic conductivity of holmium hafnate pellets is not much affected by the sintering conditions but the TSS process is the better route for processing the

holmium hafnate as the pellet can be sintered to remarkably high densities at lower temperature and exhibit lesser grain growth.

Keywords: *Sintering, densification, two step sintering, impedance spectroscopy, ionic conductivity, activation energy, holmium hafnate*

Introduction

Lanthanide based ternary oxides $Ln_2B_2O_7$ (Ln = Lanthanides, B = Hf^{4+}, Zr^{4+}) with pyrochlore structure have recently attracted increasing interest due to their structural flexibility, which can be altered by varying the processing conditions or doping and their ability to accommodate trivalent and tetravalent cations in equimolar ratio over a wider size range [1]. As a result they tend to exhibit interesting electro-physical properties such as $r_{(Ln3+)}/r_{(M4+)}$ dependent ionic conductivity [2-4], order-disorder phase transitions [5-11] and geometrically frustrated magnetism [12]. Furthermore, these materials display potential for a range of technological applications such as solid electrolytes in high temperature solid oxide fuel cells [2-4], thermal barrier coatings (TBCs) [13-15], neutron absorbing ability [16] and stable nuclear waste storage and immobilization capability [17].

Primarily, pyrochlore compounds are distinctive solid state ionic conductors and their functional properties can be altered by changing the processing conditions as well as with doping of different elements on cation sublattices [18]. It has been shown that the ionic conductivity of pyrochlore compositions increases anomalously in the vicinity of fluorite to pyrochlore structural phase transition boundary [2-4, 18]. It has been reported that $Eu_{2.096}Hf_{1.904}O_{6.952}$ and $Gd_2Hf_2O_7$ prepared using a solid state ceramic route at higher temperature of 1600 ºC and 1670 ºC [19] offered higher bulk conductivity of 5×10^{-3} Scm^{-1} and 3×10^{-3} Scm^{-1} at 780ºC, respectively suggesting that the processing temperature has profound effect on the electrical response. Similarly, $Nd_2Hf_2O_7$, $Nd_2(Hf_{2-x}Nd_x)O_{7-x/2}$ (x = 0.1) prepared using ceramic route and sintered at 1600 °C and 1700 °C exhibited considerably lower

values of 1.25×10^{-6} Scm^{-1} and 1×10^{-4} Scm^{-1}, respectively at 700 °C [20]. This may be partly due to the inhomogeneous microstructure of the Nd-hafnates. There is a paucity of literature about nanoparticle synthesis, processing, sintering and physical as well as electrical characterisation of $Ho_2Hf_2O_7$. Polycrystalline powder of $Ho_2Hf_2O_7$ has been prepared mechanochemically [21, 22] and thermodynamically [23] for metal-oxide semiconductor devices [22] and electrochemical devices [22]. Leeds Alginate Process (LAP) is an environmentally friendly, carbon neutral, facile sol-gel technique developed and researched by Kale and co-workers [24, 25] for the preparation of nanoparticles of single phase multicomponent oxide of functional ceramics at temperatures below 600 °C. This process is known to yield reproducibly and consistently homogeneous and pure single phase materials [24, 25] with good control over stoichiometry of multicomponent metal oxide nanoparticles [26]. We have recently synthesised for the holmium hafnate ($Ho_2Hf_2O_7$) nanoparticles, with cubic defect-fluorite structure, below 600°C through LAP and reported its structural and morphological properties [27]. We have also reported on the synthesis and characterisation of holmium zirconate ($Ho_2Zr_2O_7$) [28] and on the influence of processing conditions on ionic conductivity [29]. Holmium zirconate has been shown to be a reasonably good oxide ion conducting solid electrolyte with an activation energy for conduction slightly better than the conventional solid electrolytes such as yttria stabilized zirconia (YSZ) and gadolinium doped ceria (GDC) [30].

As a part of our continuing quest for new solid electrolyte materials having enhanced thermodynamic stability and, improved physico-chemical and conducting properties, we report our results of the optimising the densification of compacted nanopowders of $Ho_2Hf_2O_7$ by the conventional; SSS and unconventional; TSS techniques and their ionic conductivity as a function of temperature [31]. The microstructure and the grain growth due to sintering of compacts over the range of 1100 °C to 1500 °C are characterised. We also report on the

investigation of the effect of processing conditions and microstructure on the bulk and grain boundary conductivities of sintered $Ho_2Hf_2O_7$ pellets using ac impedance spectroscopy over the frequency range of 100 mHz to 100 MHz and temperature range of 340 °C to 750 °C.

Experimental Detail

Nanopowders of high purity single phase holmium hafnate synthesised using LAP has described in our earlier work [27] were pressed into pellets of approximately 13 mm diameter and 1.5 mm thickness in a steel die using a uniaxial press at 5 kN load. A number of pellets in the first set were processed using the conventional single step sintering (SSS) technique in the ambient environment from 1100 °C to 1500 °C with an interval of 100 °C for 2 h at each temperature with the heating and cooling rate of 3 °C/min. In the second set, several pellets were processed using the two step sintering (TSS) technique [31]. Here, the pellets were heated at 3°C /min to 1500 °C for 5 min dwell time in first step and then cooled to 1300 °C, and held at this temperature for a further 96 h in the second step to achieve maximum densification without further grain growth through diffusion process. The temperature of 1300 °C selected in the second step corresponds to 75% of theoretical density. Different sintering temperatures (1200 °C, 1300 °C) in the second step and time intervals (72 h, 96 h) were employed for the TSS process to determine the optimum sintering conditions to achieve maximum relative density with minimum grain growth.

Bulk density of $Ho_2Hf_2O_7$ pellets, processed by the SSS and TSS techniques was measured using the Archimedes' principle and the relative density was calculated on the basis of theoretical density obtained from the powder X-ray crystallography data. Density bottle with the volume of 50 ml was used to measure the bulk density. By using the Archimedes' principle, the volume of the pellet can be measured by the mass of the overflowing liquid. Equation (1) and (2) were used to measure the bulk density of sintered pellets:

$$D = \frac{W_3 - W_1}{(W_2 - W_1)/_{D_w} - (W_4 - W_3)/_{D_w}} \quad (1)$$

where,

W_1 = Mass of the dry bottle W_2 = Mass of the bottle filled with liquid

W_3 = Mass of the bottle with pellet, W_4 = Mass of the bottle with pellet and the liquid

D_w = Density of the liquid D = Density of pellet

Since the liquid used in this study is water with the density 1 g/cm^3, equation (1) reduced to equation (2)

$$D = \frac{W_3 - W_1}{(W_2 - W_1) - (W_4 - W_3)} \quad (2)$$

The microstructure of holmium hafnate pellets sintered by the above two processes was studied by scanning electron microscopy (SEM) using a Hitachi SU8230 and the grain growth was analysed using ImageJ software. Processed pellets were ground, finely polished using standard metallography techniques and thermally etched before performing SEM analysis. Pellets were ground to remove the top layer before polishing with 3 um diamond paste to achieve the smooth surface finish. All the sintered and polished pellets were thermally etched by heating them for 1 hr at the temperature 50 °C below their respective sintering temperature, i.e. if pellet sample is sintered at 1200 °C then thermal etching is done at 1150 °C.

Preparation of samples for ac impedance spectroscopy were carried out by coating the both faces of each of the processed pellet with conductive silver paste and firing at 800 °C for 1 h to remove any binder present in it and to metallise the contact surfaces in order to minimise interfacial impedance between the sample surface and platinum measuring leads. The frequency range of 100 mHz to 100 MHz with an excitation voltage of 10 mV, using a Solartron SI1260 impedance analyser, was employed for the impedance measurements as a function of temperature between 340 °C to 750 °C. Before carrying out the measurement the samples were

heated to the desired temperature at the rate of 3 °C/min and to achieve the thermal equilibrium kept at that temperature for 30 mins. The pellets were spring loaded in a bespoke quartz rig during the impedance measurements to provide a firm contact between the sample surface and measuring leads. A K-type thermocouple is placed close to the sample adjacent to the rig for monitoring the stabilization of temperature. The quartz rig was housed in a Faraday cage within a horizontal tube furnace in order to prevent the electric field from the furnace wire windings affecting impedance measurements. Z-plot was used to control the impedance analyser, while the data were analysed using Z-view (Scribner Associates) and plotted in Origin Pro software.

Results and Discussion

Sintering and Microstructure

The relative density of the samples sintered from 1100 °C to 1500 °C with the SSS process is shown in Fig. 1. The relative density was found to be in the range of 74 (±0.5)% to 93 (±0.5)% depending on the sintering temperature. There is a mere 1.2 % increase in relative density between the sample pellet sintered at 1400 °C and 1500 °C. Furthermore, there is an increment of just 0.8 % in the relative density with the increase in sintering duration from 2 h to 6 h at 1500 °C as clearly seen in Fig. 1. This clearly suggests that an optimum sintering temperature and time for $Ho_2Hf_2O_7$ nanopowders obtained in this study is 1500 °C for 2 h using SSS process. Higher densification of $Ho_2Hf_2O_7$ pellets achieved by sintering at 1500 °C for 2 h is significantly higher than that of mechanochemically obtained holmium hafnate sintered at 1500 °C for 12 h (84.23 %) [21].

In first attempt of application of TSS process to $Ho_2Hf_2O_7$, pellets were sintered in two steps (I) –1500 °C for 5 min, (II) – 1200 °C for 24 h as densities higher than 75 % were adequate for second sintering step [31]. The relative densities achieved in the second step for 24 h and 72 h dwell time were 84 (±0.5) % and 92 (±0.2) %, respectively. Since the relative densities achieved were even less than that achieved at 1500°C for SSS process subsequent pellets were

sintered using the TSS process at (I) –1500 °C for 5 min, (II) – 1300 °C for 72 h and a significant rise in relative density was noticed. The sintering duration in the second step was increased to 96 h to achieve maximum density and relative density of 98 (±0.1)% was successfully achieved which is considered to be good for solid electrolyte applications. The corresponding residual porosity of pellets was reduced from 25 (±0.5)% to 6 (±0.5)% in the SSS process and further down to 2 (±0.1)% in the TSS process as shown in Fig. 1.

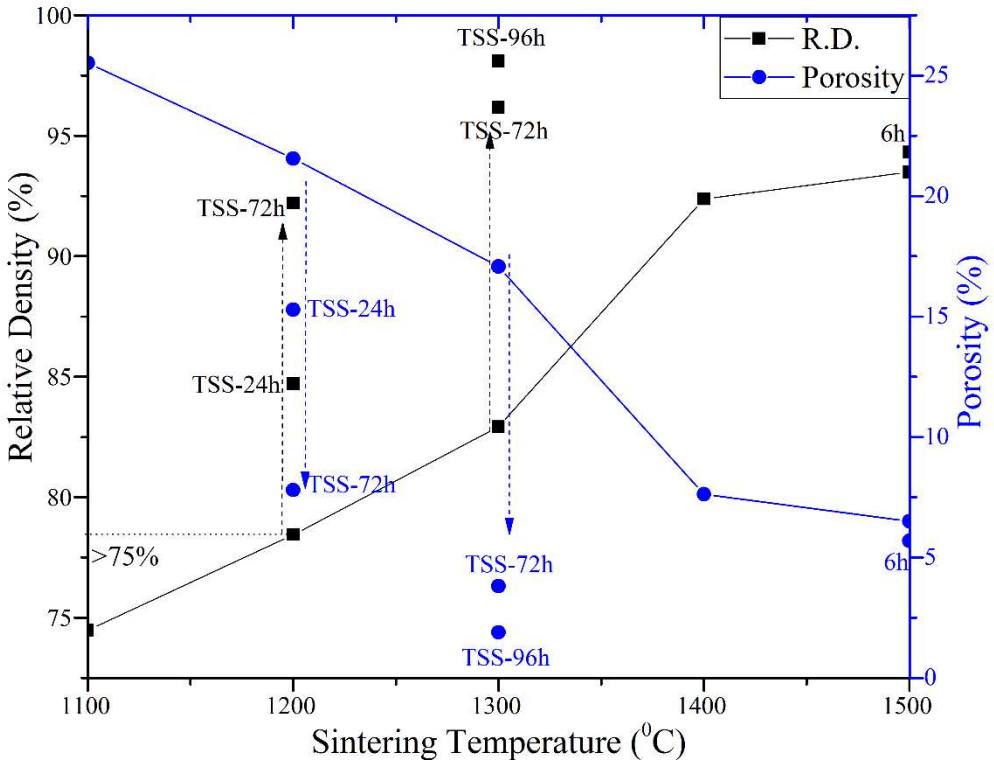

Fig. 1: Effect of sintering temperature on the relative density and porosity of holmium hafnate pellets. Two step sintering (TSS): (I) – 1500 °C for 5 min, (II) -1300 °C for 96 h. Arrows showing increase in relative density and decrease in porosity with TSS process.

The microstructure of pellets sintered using SSS process from 1100 °C to 1500 °C and TSS process (I) –1500 °C for 5 min, (II) – 1300 °C for 96 h were analysed by scanning electron microscopy (SEM). SEM micrographs of sintered pellets are shown in Fig. 2. Furthermore, a representative SEM image exhibiting a dense microstructure of the pellet sintered using the TSS process at a lower magnification is shown in Fig. 3 for comparison of the structure of the

sample over a larger area relative to that shown in Fig. 2(f). It is clearly seen that the microstructure shown in Fig. 2(f) is in reasonably good agreement with that shown in Fig. 3. Effect of sintering temperature on the relative density and grain size is shown in Table 1. Grain size was calculated from SEM mircrographs using ImageJ and it was found that with the increase in sintering temperature from 1100 °C to 1500 °C for the SSS process the grain size also increased and reached a maximum of 1.6 (±0.02) μm at 1500°C, as shown in Table 1 while the corresponding relative density gradually increased up to a maximum value of 93 % after attaining a nearly stable value as seen in Fig. 1.

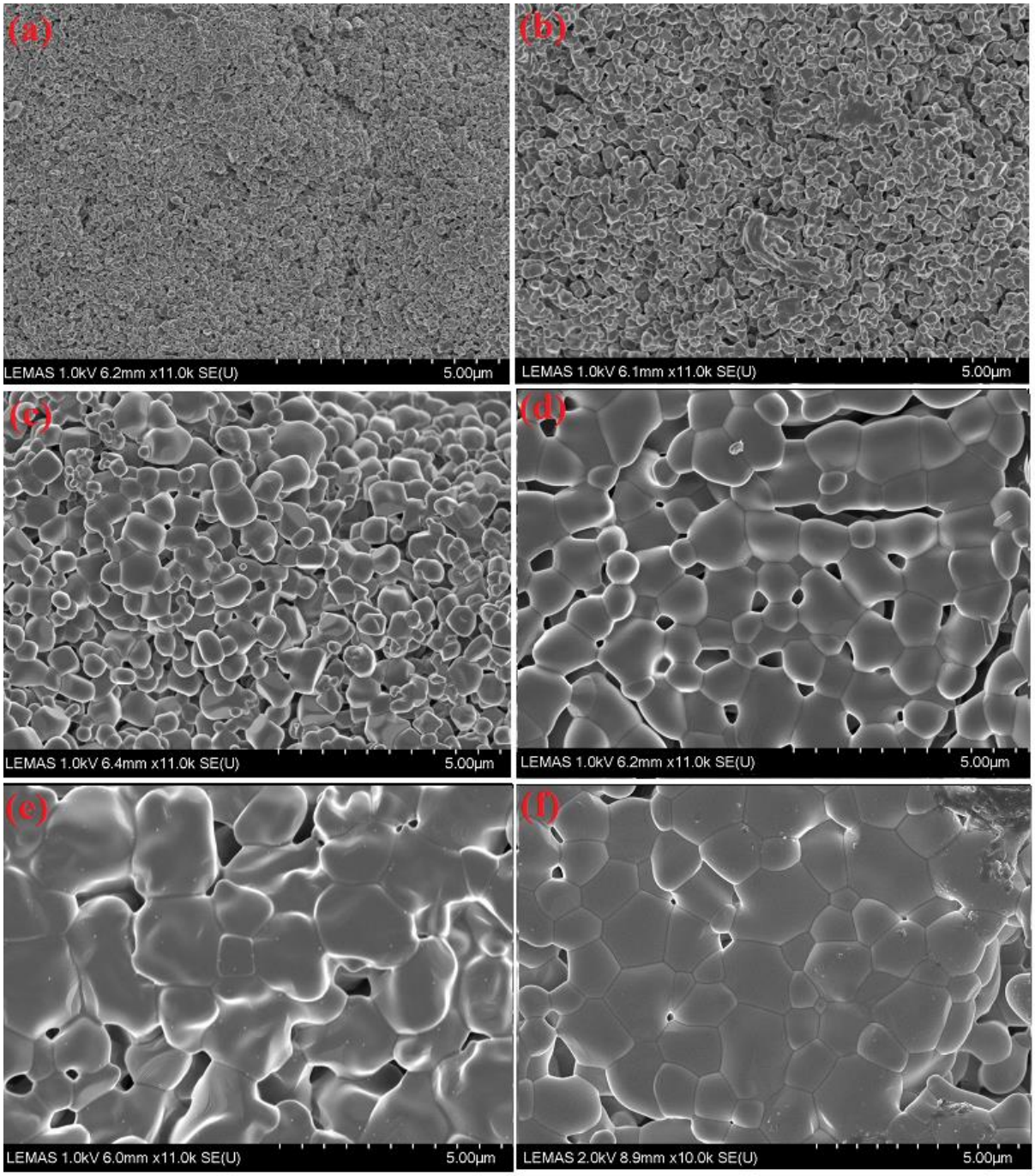

Fig. 2: SEM micrographs of sintered $Ho_2Hf_2O_7$ pellets. From (a) to (e) are the micrographs of the pellets after the conventional SSS technique for 2h at (a) 1100 °C (b) 1200 °C (c) 1300 °C (d) 1400 °C (e) 1500 °C and (f) after unconventional TSS technique: (I) – 1500 °C for 5 min, (II) – 1300 °C for 96 h.

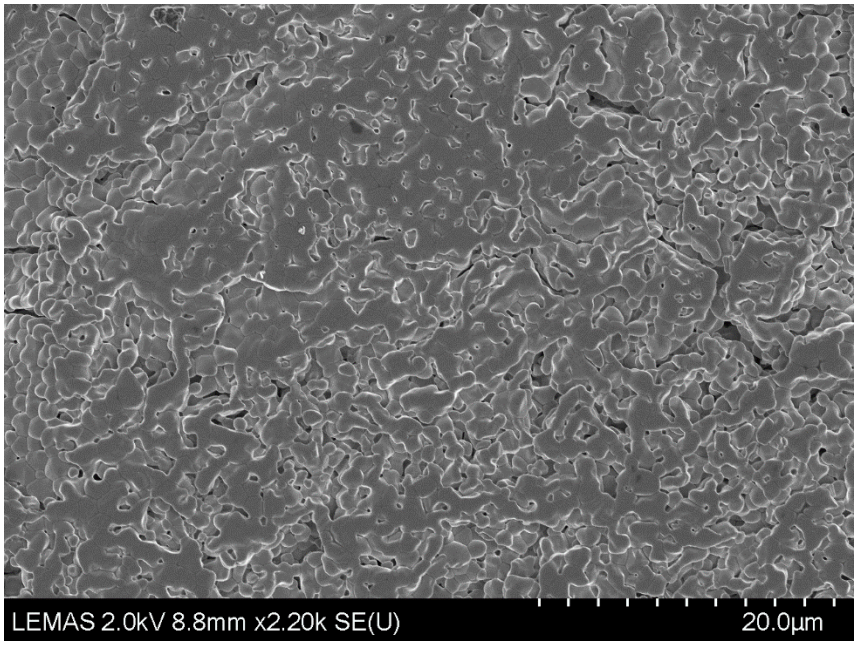

Fig. 3: Lower magnification SEM micrograph of pellet sintered using TSS process

Pellets sintered using the TSS process achieved a higher density of 98 % and grain size of 0.77 (±0.02) µm, almost 50 % smaller than the sample in Fig. 2 (e). There is substantial increase in densification with the TSS process, but an increase of 0.18 (±0.02) µm in grain size was noticed as compared to the one found at 1300 °C with the SSS process (Fig. 2 (c)). The increase in grain size with the TSS process was mainly due to the grain coarsening occurring in first sintering step [31] since the sintering temperature was 200 °C higher though for only 5 mins compared with the sample sintered using SSS process at 1300 °C. It is observed that in the second step of TSS process densification proceeds without grain growth suggesting that the grain boundary diffusion is the active mechanism while the grain boundary migration is suppressed [31].

Therefore it can be suggested that the TSS process for sintering of $Ho_2Hf_2O_7$ pellets is more favourable for achieving the high densification while curbing the grain growth compared with the SSS process, where the densification is lower and the grain growth is higher as seen in Table 1.

Table 1: Variation of grain size and relative density as a function of sintering temperature of $Ho_2Hf_2O_7$ pellet samples.

Sintering Temperature (°C)	Relative Density (%)	Grain Size (μm)
1100	74.48	0.122
1200	78.44	0.218
1300	82.93	0.590
1400	92.37	1.011
1500	93.50	1.591
TSS	98.10	0.770

X-ray Diffraction (XRD) analysis was performed on the sintered pellets of holmium hafnate. Fig. 4 shows the XRD patterns of $Ho_2Hf_2O_7$ pellets sintered at 1200 °C, 1500 °C and with TSS process. Holmium hafnate pellets sintered at 1500 °C by SSS and TSS process clearly adopts a fluorite structure [32] however minor superstructure peaks of pyrochlore were observed when sintered at 1200 °C. Pyrochlores are superstructure of an anion-deficient fluorite atomic arrangement, its diffraction pattern have set of superstructure reflections in addition to characteristic peaks of fluorite substructure [33]. Factors which affect the intensities of superstructure reflections are degree of ordering, distribution of oxygen vacancies and the difference of average scattering factors of elements involved [21]. However, at 1500 °C and with TSS process clean XRD pattern of holmium hafnate with stable fluorite structure was obtained which were subsequently used for ac impedance measurements as a function of temperature. At these temperatures and processing conditions no superstructure reflection of pyrochlore was observed as seen in Fig. 4. Here the sharp peaks without any superstructure

pyrochlore reflection are assigned to their miller indices with fluorite structured holmium hafnate.

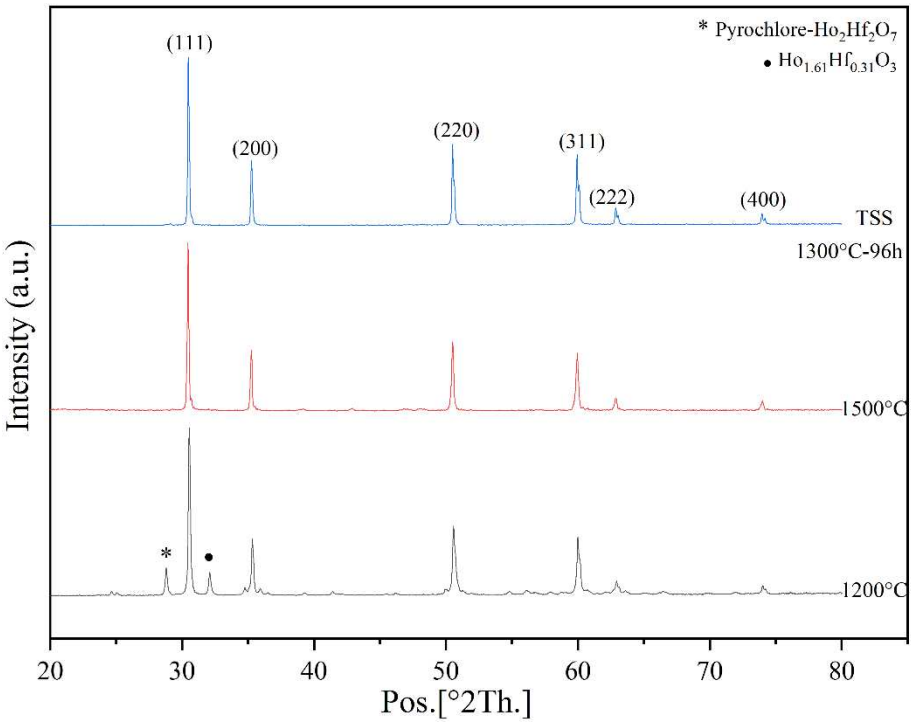

Fig. 4: XRD patterns of sintered holmium hafnate pellets. The patterns for 1200 °C, 1500 °C and TSS are indexed by ICDD, 00-024-0473 with defect fluorite cubic $Ho_2Hf_2O_7$ shown at the top of the peaks. Tick marks 'asterisks' for $Ho_2Hf_2O_7$ and 'filled circles' for $Ho_{1.61}Hf_{0.31}O_3$ minor phase reflections.

Table 2 shows the effect of temperature increase in crystallite size and unit cell parameters of holmium hafnate. With the increase in temperature the crystallite size increased to 109 nm at 1500 °C and corresponding decrease in microstrain was observed as shown in Table 2. Increasing in sintering temperature results in narrowing of diffraction peaks which is due to growth in crystallite size. Unit cell parameters was found to remain nearly constant (~5.131-5.148 A˚) with the increase in sintering temperature and they are in conformation of fluorite phase. These results show that $Ho_2Hf_2O_7$ maintains stable fluorite structure over the wide temperature range as predicted by the Ho^{3+}/Hf^{4+} cation radius ratio [23].

Table 2: Effect of temperature on crystallographic data and structural refinement parameters of holmium hafnate pellets

Temperature, °C	700-Nanopowder [27]	1200	1500	TSS
Phase	Defect-Fluorite	Defect-Fluorite	Defect-Fluorite	Defect-Fluorite
Space group	$Fm\bar{3}m$	$Fm\bar{3}m$	$Fm\bar{3}m$	$Fm\bar{3}m$
Lattice constant, A° a=b=c	5.131	5.147	5.148	5.147
R_p, %	2.09	15.6	11.9	17.3
R_{wp}, %	2.84	23.0	15.2	21.0
R_{exp}, %	2.45	10.37	11.2	12.5
GOF, x^2	1.34	4.94	1.84	2.82
Crystallite Size, nm	6.0	65	109	93
Micro Strain, %	1.18	0.25	0.10	0.14

Furthermore, Table 2 also presents the Rietveld refinement parameters of the sintered $Ho_2Hf_2O_7$ pellets. The values of R_{wp} and Goodness of Fit (GOF) relative to temperature are

tabulated. Goodness of Fit (x^2) is ratio of squares of R_{wp} and R_{exp}, $x^2 = R_{wp}^2 / R_{exp}^2$, and for acceptable fit parameters its value must be less than 10 [34, 35]. Lower values of GOF for the samples prepared at 700 °C, 1500°C and with TSS process confirms an excellent agreement between experimentally recorded and calculated XRD pattern during the Rietveld refinement. At 1200 °C comparatively higher values show more residual data after refinement which is due to the appearance of minor pyrochlore superstructure reflections.

Ac Impedance Spectroscopy

Impedance spectroscopy of $Ho_2Hf_2O_7$ pellets sintered in the SSS process was carried out over the temperature range of 340 °C to 750 °C in the frequency range of 100 mHz to 100 MHz for both heating and cooling cycles. Nyquist plots at selected temperatures are shown in Fig. 5, which are used to analyse relaxation phenomena such as contribution of bulk, grain boundary and electrode interface effect towards the ionic conductivity. At 340 °C a single semicircle was observed for both heating and cooling cycles as shown in Fig. 5 (a) which is an indication of predominant bulk contribution.

In contrast at 550 °C two semi-circles were recorded for both heating and cooling cycles as shown in Fig. 5 (b). The first high frequency semi-circle (left) was attributed to the bulk or grain interior response, whereas the second low frequency semi-circle (right) attributed to the grain boundary response. The contribution of the grain boundary to the total resistance increased with the increase in temperature from 340 °C to 750 °C. The temperature dependence of the resistivity (ρ) and the conductivity (σ) were calculated by fitting the impedance data to the equivalent circuits shown in the inset of Figs. 5 (a) and 5 (b) using the dimensional constants of the pellet sample. Frequency dependence of the impedance was modelled using constant phase element (CPE) to account for the possible chemical, surface and structural inhomogeneity in the sample. The constant phase elements (CPE) represent the non-ideal capacitive contributions of the transport processed in the bulk (CPE_b) and at the grain

boundaries (CPE_{gb}). The CPE has actually two parameters the one is capacitance (C_{CPE}) and an exponent (n) which varies between 0.5 and 1. CPE is a capacitor if the value of n is 1 and a 45 degree line is produced in the complex impedance plot for n equal to 0.5 [36, 37].

The equivalent circuit in Fig. 5 shows that the CPE is in parallel to the resistor which is the representation of semicircle (Cole element). The capacitance associated with the high-frequency semicircle in Fig. 5b for SSS processed pellet is found to be around 2.05×10^{-11} F and the one associated with the lower frequency semicircle is 3.83×10^{-8} F. The high-frequency arc can therefore be identified as a bulk property since its capacitance is in pF order [38] and the value of n reduced to 0.97 whereas the lower frequency arc can be identified as the grain boundary resistance as its capacitance is in nF range [38] and the value of n is found to be 0.72.

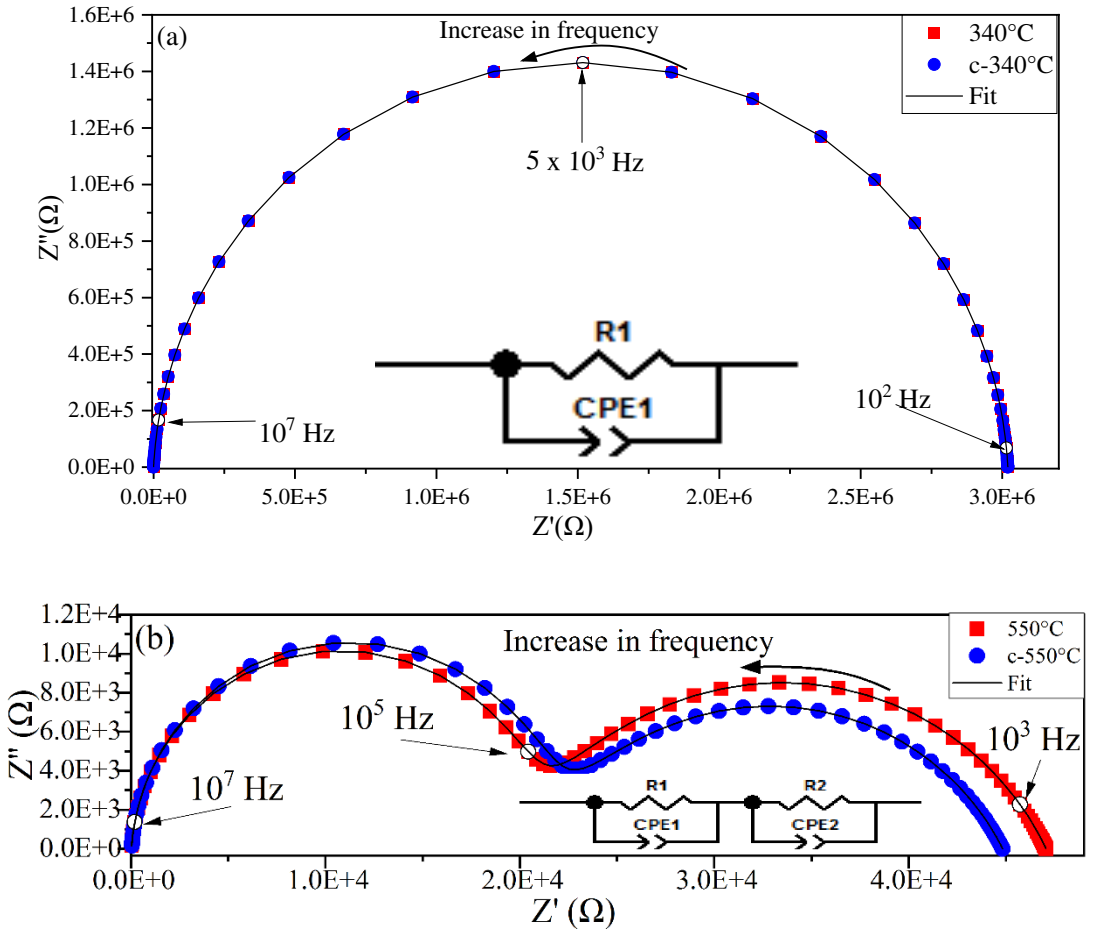

Fig. 5: Complex impedance plots for $Ho_2Hf_2O_7$ sintered at 1500 °C for 2 h measured in heating cycle at (a) 340 °C and (b) 550 °C, (c-340 °C and c-550 °C for cooling cycle) with equivalent circuits to fit the data.

Fig. 6 shows the evolution of impedance spectra of the pellets with the increase in temperature from 400 °C to 750 °C for SSS processed sample. It is interesting to note that the grain boundary contribution to the conductivity is seen only beyond 500 °C. The equivalent circuit shown in the inset of Fig. 5 (a, b) have been used to model the frequency response of the sample in this study over the entire temperature range of measurement.

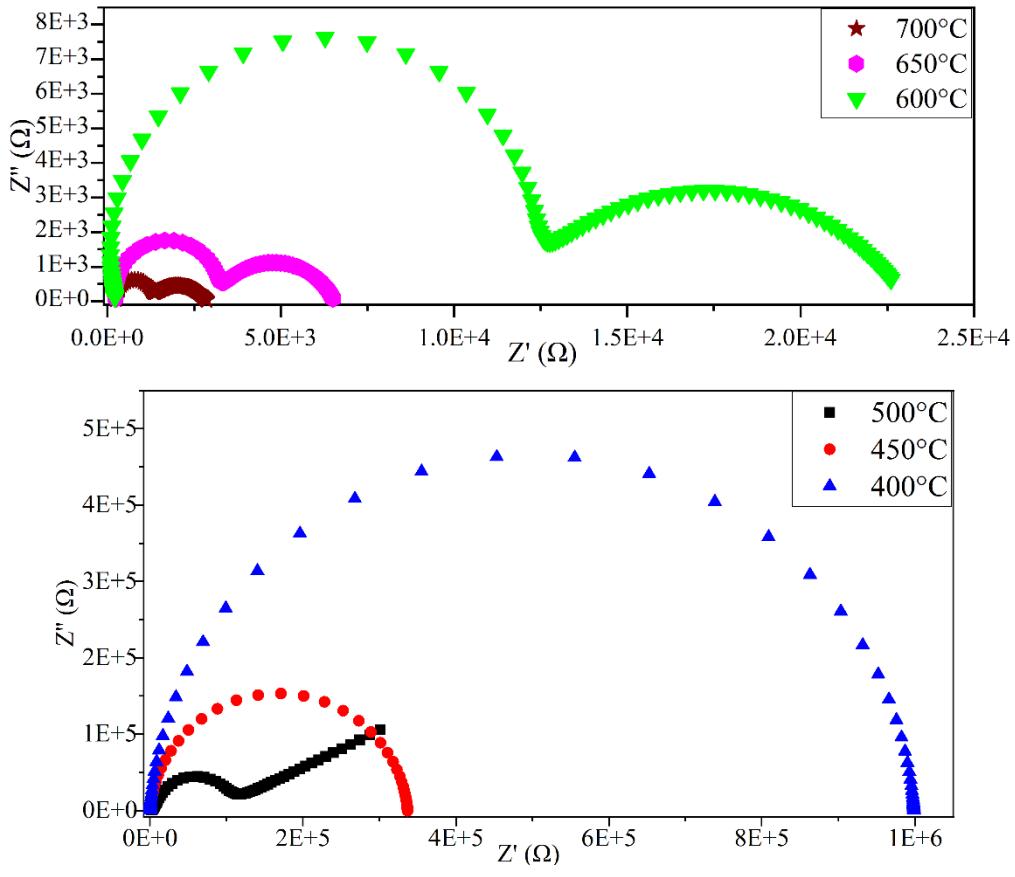

Fig. 6: Evolution of impedance spectra with temperature for SSS processed pellet. Frequency increases from right to left.

The temperature dependence of the electrical conductivity was analysed by fitting to an Arrhenius expression of the form shown in equation (3)

$$\sigma T = \sigma_0 \, exp \, (-E_a/\mathrm{k}T) \quad (3)$$

where σ_0 is pre-exponential factor related to the effective number of mobile charge carriers, T is the absolute temperature, k is Boltzmann constant and E_a is the activation energy for oxide ion migration. The value of activation energy for ionic conduction in $Ho_2Hf_2O_7$ has been obtained by plotting $log\sigma T$ against $1/T$ as shown in Fig. 7 for bulk and grain boundary effects of single step sintered $Ho_2Hf_2O_7$ pellet measured over the temperature range of 340 °C to 750 °C and frequency range of 100 mHz to 100 MHz for both heating and cooling cycles. The straight lines in the graph represents the experimental data from both heating and cooling cycles fitted using a least square best fit software to an Arrhenius expression confirming that the ionic diffusion in the sample is thermally activated. Activation energies for both bulk and grain boundary diffusion are calculated from the slopes of best fit linear equations from the respective data sets.

According to calculations, the energetically preferred pathway for oxide ion migration in $A_2B_2O_7$ pyrochlore [39, 40] consists of $O_{48f} \rightarrow O_{48f}$ sequential jumps, along the shortest edge of the BO_6 polyhedra such as HfO_6. In this study the activation energies found for the bulk and grain boundary conductivity of SSS processed $Ho_2Hf_2O_7$ pellet has been found to be 0.54 (±0.01) eV and 0.61 (±0.01) eV, respectively. The values of bulk and grain boundary conductivities found at 750 °C are 2.44×10^{-4} S.cm^{-1} and 1.22×10^{-4} S.cm^{-1}, respectively. The value of conductivity of $Ho_2Hf_2O_7$ (5.01×10^{-4} S.cm^{-1}) obtained in a recent study at 750 °C [21] is in reasonable agreement with that measured in this study at the same temperature suggesting high degree of reliability and accuracy of our measurement procedure.

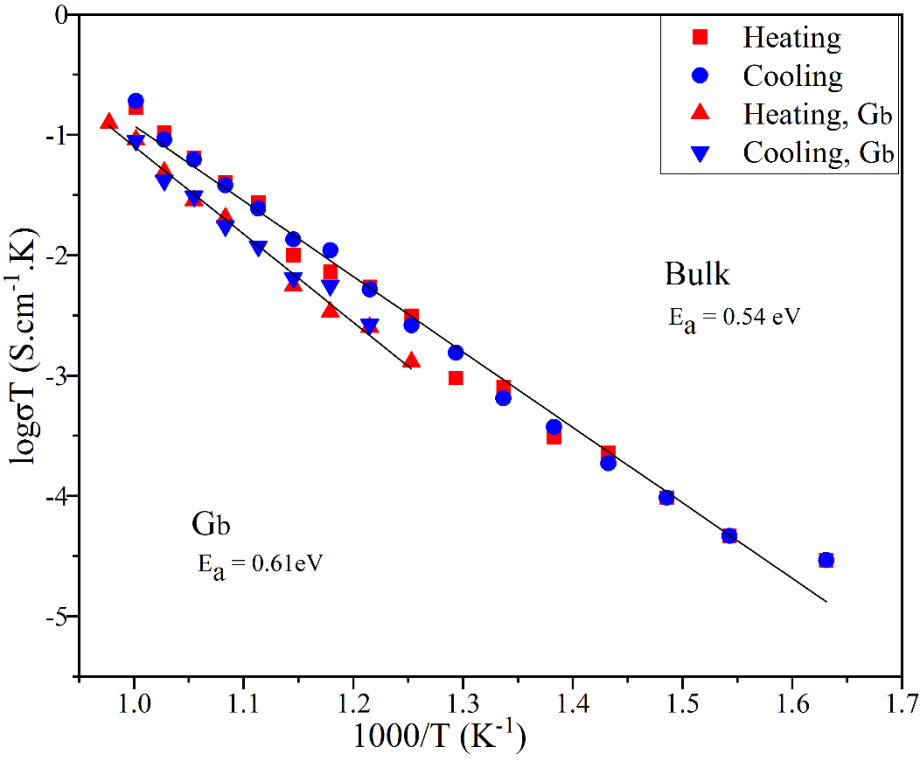

Fig. 7: Temperature dependence logarithm of (σT) of bulk and grain boundary in heating and cooling cycles of holmium hafnate pellets sintered at 1500 °C for 2h using SSS process.

Results of impedance spectroscopy of $Ho_2Hf_2O_7$ pellets measured at 350 °C and 550 °C on samples sintered using the TSS process are shown in Figs. 8 and 9. It can be seen that the Nyquist plots for the sample sintered using TSS process appear similar to those shown in Figs. 5 and 6 for samples sintered using SSS process.

The capacitance associated with the high-frequency semicircle in Fig. 8b for TSS processed pellet is found to be around 1.21×10^{-11} F with the value of n reduce to 0.98 and identified as the bulk contribution to the overall conductivity. The capacitance associated with the lower frequency semicircle is 3.54×10^{-8} F and the value of n equals 0.73 and identified as the grain boundary contribution [38].

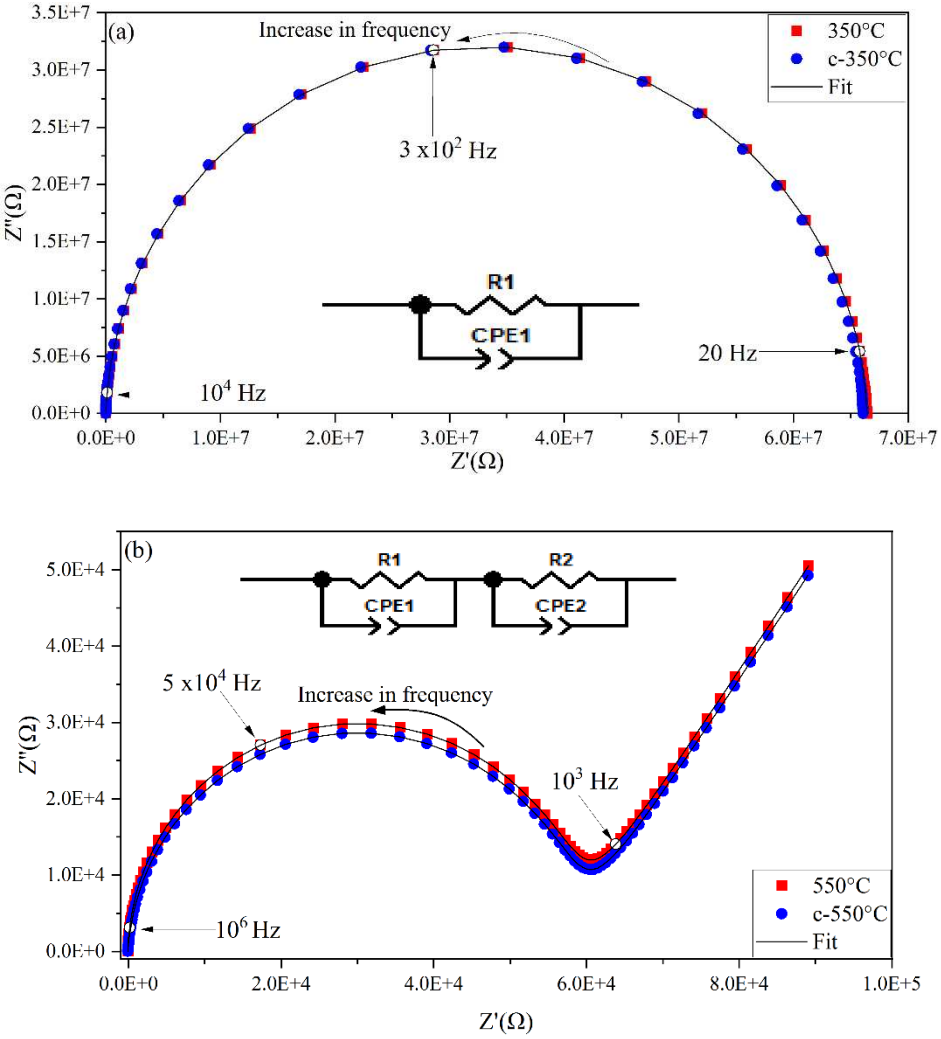

Fig. 8: Complex impedance plots for $Ho_2Hf_2O_7$ with two step sintering; (I) – 1500 °C for 5 min, (II) – 1300 °C for 96 h measured in heating cycle at (a) 350 °C and (b) 550 °C, (c-350 °C and c-550 °C for cooling cycle) with equivalent circuits used to fit the data.

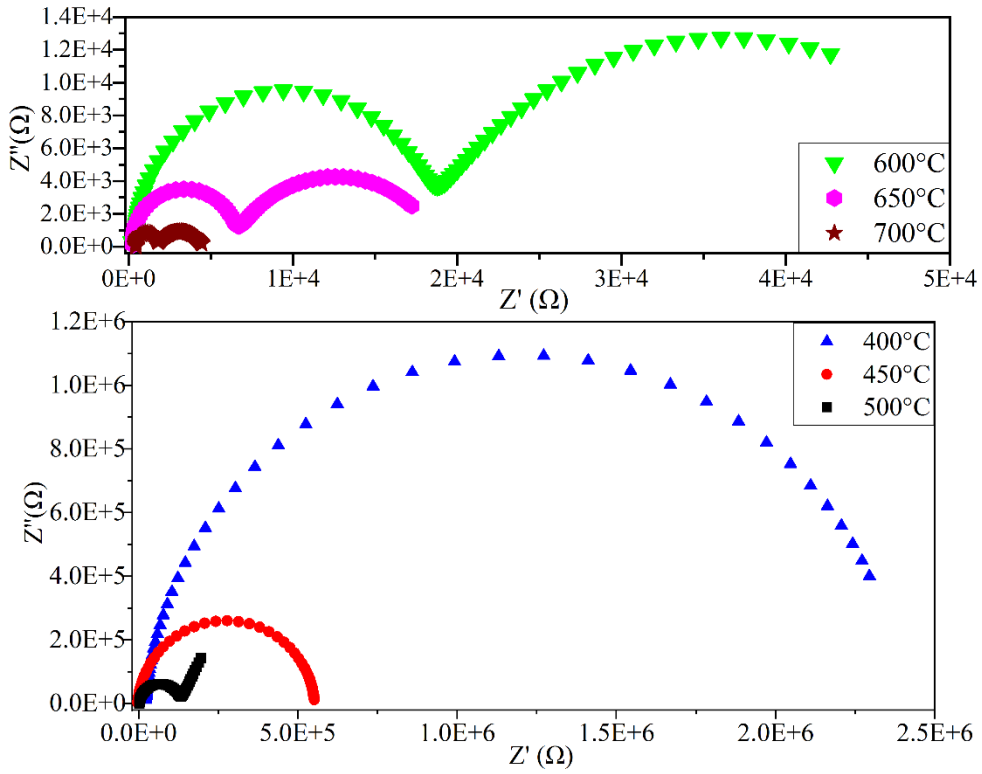

Fig. 9: Evolution of impedance spectra with temperature for the TSS processed pellet. Frequency increases from right to left.

The Arrhenius plots of bulk and grain boundary (Gb) conductivities for both heating and cooling cycles of holmium hafnate prepared using the TSS process are shown in Fig. 10. All the contribution to the total conductivity from 350 °C to 550 °C is due to the bulk conductivity. A noticeable deviation in the conductivity plot is observed at 550 °C which indicates the decrease in bulk conductivity and after that grain boundary contribution is observed at higher temperatures. Grain boundary contribution to the total conductivity was seen from 600 °C as seen from the grain boundary (Gb) plot in Fig. 9. The values of activation energies for bulk and grain boundary have been found quite close to each other, 0.59 (±0.01) eV and 0.57 (±0.01) eV, respectively. It can be seen in Fig. 10 that the bulk and grain boundary conductivity for the $Ho_2Hf_2O_7$ sample sintered by the TSS process are very similar suggesting an almost identical Gb contribution to the total conductivity.

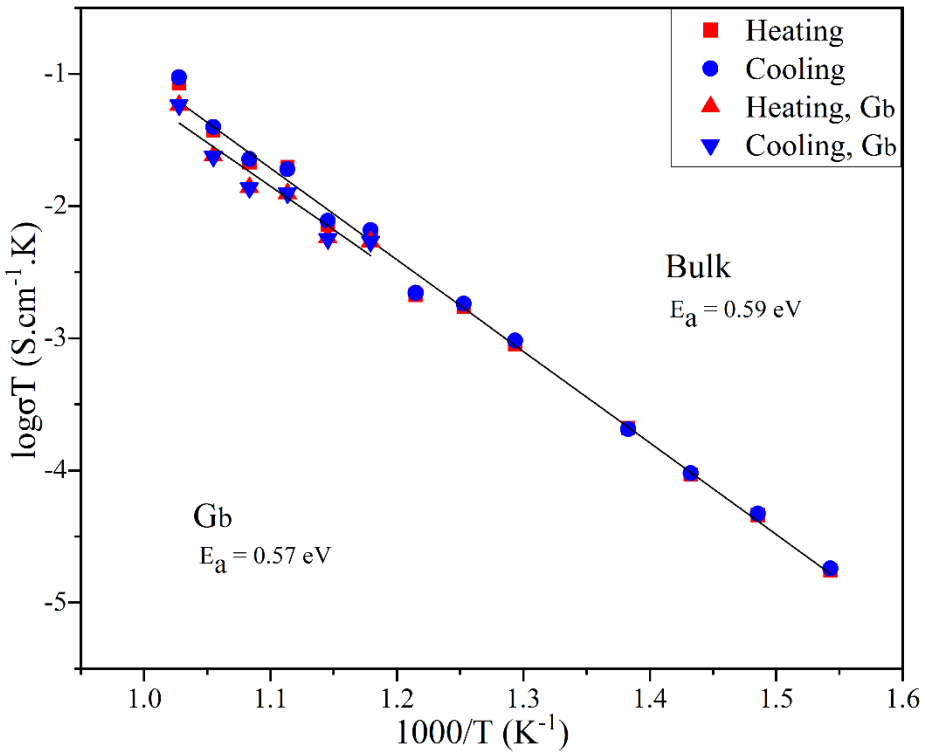

Fig. 10: Temperature dependence Arrhenius plots of bulk and grain boundary (Gb) conductivity for both heating and cooling cycles of holmium hafnate prepared using TSS process.

The Arrhenius plots for bulk conductivity of $Ho_2Hf_2O_7$ pellets sintered using the SSS and TSS processes are compared in Fig. 11 (a). The magnitude of activation energy for the samples sintered by SSS process is slightly lower in the case of bulk and slightly higher for grain boundary than that of the samples prepared by TSS process. The values of the bulk conductivity for the SSS process is half an order of magnitude higher than that of the TSS processed sample at the lower temperature end of measurement but the gap closes down with the increase in temperature which is clearly seen in Fig. 11 (a) and Table 3.

Table 3: Comparison of activation energies and conductivity values of SSS and TSS processed $Ho_2Hf_2O_7$

Sample	Activation Energy (eV)	R^2 value	Conductivity at 575 °C S.cm^{-1}	Conductivity at 700 °C S.cm^{-1}
SSS-Bulk	0.54	0.98484	1.08×10^{-5}	1.00×10^{-4}
SSS-Gb	0.61	0.9872	5.28×10^{-6}	4.66×10^{-5}
TSS-Bulk	0.59	0.99457	7.58×10^{-6}	9.19×10^{-5}
TSS-Gb	0.57	0.93531	6.34×10^{-6}	5.94×10^{-5}

Fig. 11 (b) shows the comparison of Arrhenius plots of grain boundary conductivity of SSS processed $Ho_2Hf_2O_7$ samples with TSS processed samples. Compared with the rest of the data presented in Figs. 11(a, b), there is a noticeably large scatter in the data of grain boundary conductivity over the temperature range for TSS processed sample resulting in the decrease in R^2 value for linear fit as shown in Table 3.

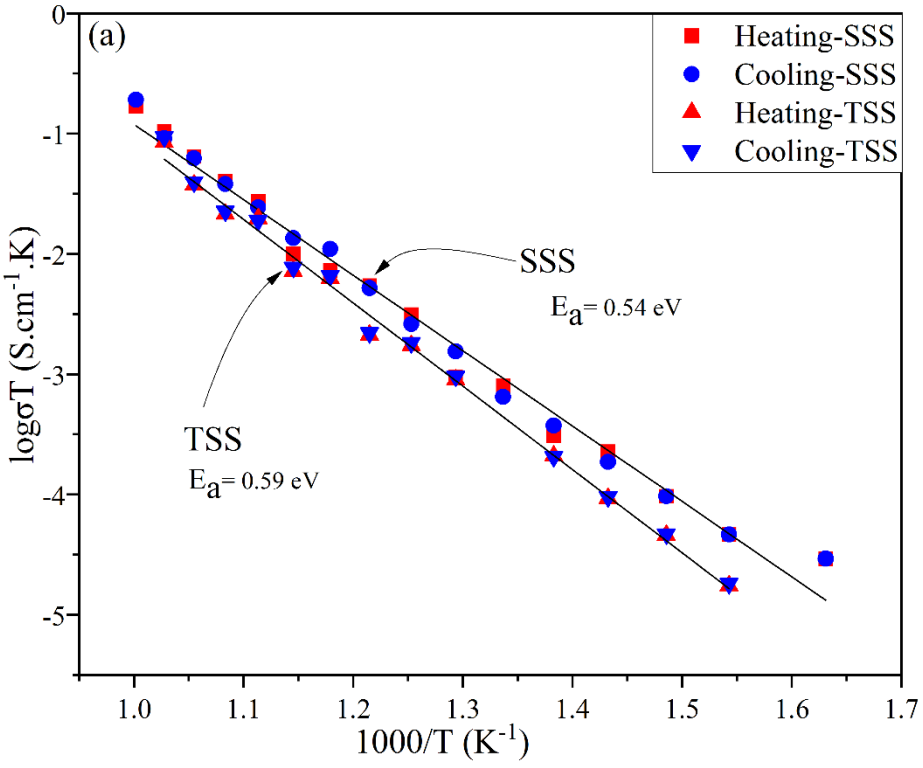

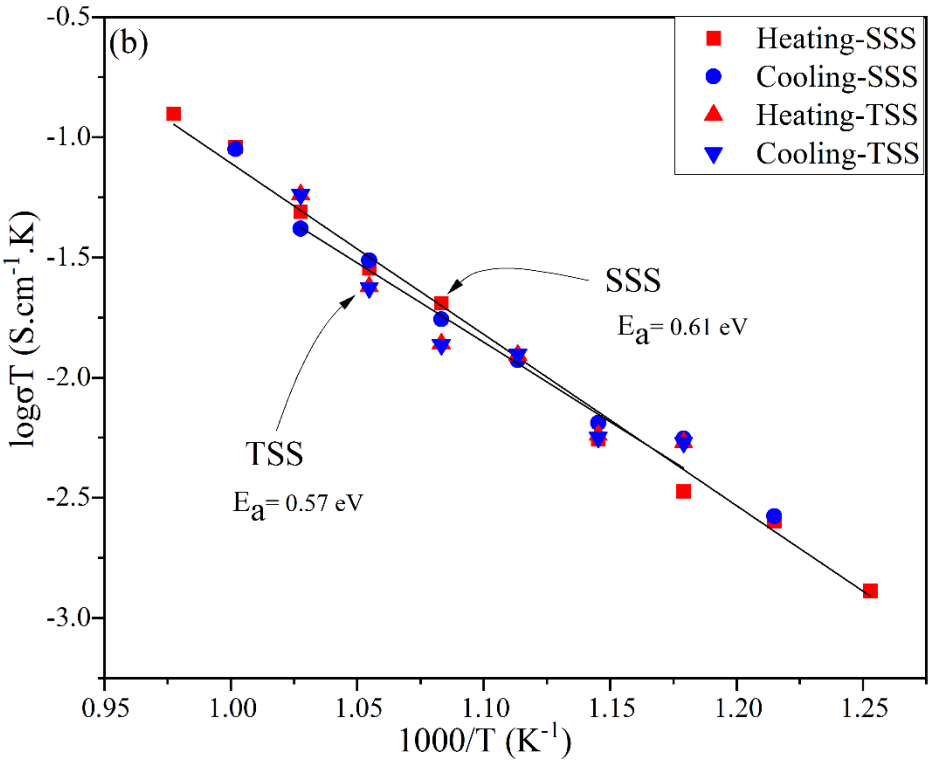

Fig.11: Comparison of temperature dependence Arrhenius plots of (a) bulk and (b) grain boundary (Gb) conductivity for both heating and cooling cycles of holmium hafnate prepared using SSS and TSS processes.

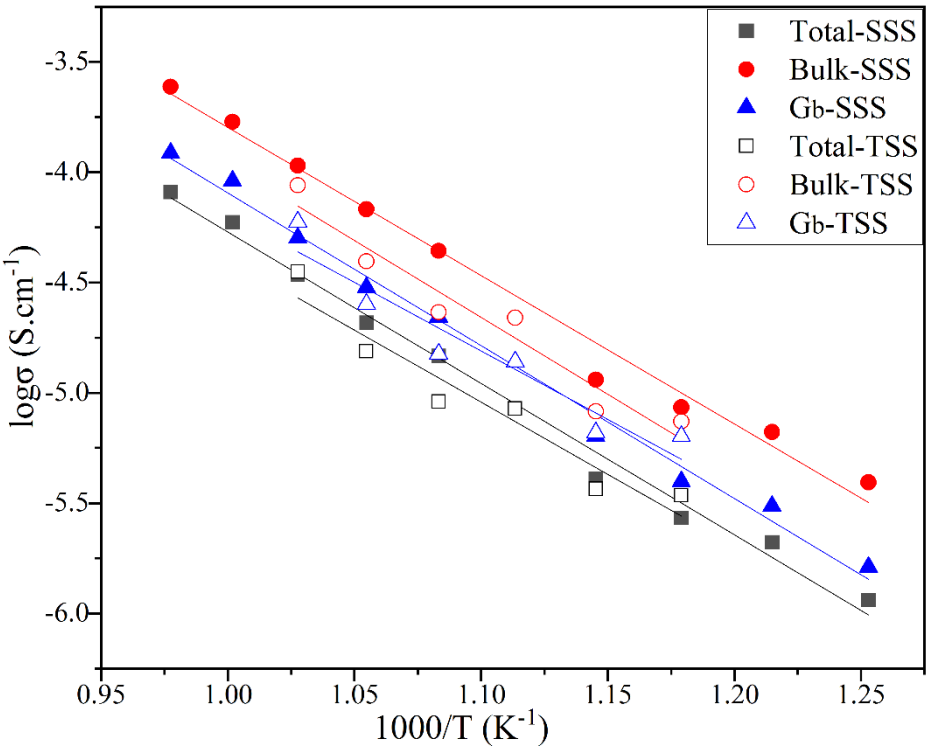

Fig. 12: Comparison of total, bulk and grain boundary conductivity of SSS and TSS processed pellets

Fig. 12 compares the total, bulk and grain boundary conductivity of pellets sintered using SSS and TSS processes. Above comparison suggests that although the SSS processed $Ho_2Hf_2O_7$ sample exhibits slightly better results than that of TSS processed sample, the difference in the results are insignificant compared to that observed in the case of $Ho_2Zr_2O_7$ [29] samples synthesised and processed employing similar techniques. This suggests that since the physical properties such as density, grain size and sintering temperatures of samples sintered using TSS process are consistently better than SSS processed samples in most ceramic materials it is better to employ TSS process for processing nanopowders of ion-conducting ceramics for electrochemical applications.

Conclusions

Nanopowders of holmium hafnate ($Ho_2Hf_2O_7$) [27] produced by Leeds Alginate Process (LAP), were compacted into pellets and sintered through single step sintering (SSS) and two step sintering (TSS) routes and the effect of processing conditions on the microstructure and ionic conductivity has been analysed. High density $Ho_2Hf_2O_7$ ceramic is successfully obtained through the TSS process having lower grain growth. The TSS process is found to be a better route for ceramics processing as the relative density of the pellet reaches to 98 % at lower temperature (1300 °C) with lesser grain growth in comparison to the densification (93.5 %) achieved through SSS process at higher temperature (1500 °C) with pronounced grain growth 1.59(±0.01) μm. The bulk and grain boundary conductivities of $Ho_2Hf_2O_7$ processed using the SSS and TSS processes were measured over the temperature range of 340 °C to 750 °C for both heating and cooling cycles using AC impedance spectroscopy in the frequency range of 100 mHz to 100 MHz. The complex impedance plots for SSS and TSS processed $Ho_2Hf_2O_7$ nanopowders exhibit consistent results for both heating and cooling cycles indicating that

$Ho_2Hf_2O_7$ responds reversibly throughout the temperature range of measurements. The values of bulk (1.00×10^{-4} $S.cm^{-1}$) and grain boundary (4.66×10^{-5} $S.cm^{-1}$) conductivities of $Ho_2Hf_2O_7$ pellets prepared using the SSS and TSS process are not distinctly different unlike in the case of $Ho_2Zr_2O_7$ [29] and therefore the main advantage of TSS process over SSS process for processing the nanopowders of $Ho_2Hf_2O_7$ is for yielding better physical properties such as lower sintering temperature, smaller grain size and higher density. The magnitude of oxide ion conductivity and the activation energy for various processes (bulk, grain boundary and total) of $Ho_2Hf_2O_7$ obtained in this study has been found to be comparable with conventionally processed $Ho_2Hf_2O_7$ [21]. Therefore, lower sintering temperature, higher densification and lesser grain growth makes the TSS process more preferred route for the processing of $Ho_2Hf_2O_7$. .

Acknowledgement

The first author would like to thank the Commonwealth Scholarship Commission (CSC), UK for the financial support, PKCA-2016-93.

Competing financial interests

The authors declare no competing financial interests.

References

[1] F.S. Galasso, 1970. Structure and properties of inorganic solids, Pergamon Press Inc.

[2] H. Yamamura, H. Nishino, K. Kakinuma, K. Nomura, Electrical conductivity anomaly around fluorite-pyrochlore phase boundary. Solid State Ionics 158 (2003) 359-365.

[3]. J.A. Dıaz-Guillen, A.F. Fuentes, M.R. Dıaz-Guillen, J.M. Almanza, J. Santamarıa, C. Leon. The effect of homovalent A-site substitutions on the ionic conductivity of pyrochlore-type $Gd_2Zr_2O_7$. J Power Sources. 186 (2009) 349–352.

[4]. J.A. Dıaz-Guillen, M.R. Dıaz-Guillen, K.P. Padmasree, A. F. Fuentes, J. Santamarıa, C. Leon, High ionic conductivity in the pyrochlore type $Gd_{2-y}La_yZr_2O_7$ solid solution ($0\leq y\leq1$). Solid State Ionics. 179 (2008) 2160–2164.

[5] M. Subramanian, G. Aravamudan, G. Subba Rao, Oxide pyrochlores: a review. Prog. Solid State Chem. 15 (1983) 55-143.

[6] J. Shamblin, M. Feygenson, J. Neuefeind, C. Tracy, F. Zhang, S. Finkeldei, D. Bosbach, H. Zhou, R. Ewing, M. Lang, Probing disorder in isometric pyrochlore and related complex oxides. Nat. Mater. 15 (2016) 507-511.

[7] P. Blanchard, R. Clements, B. Kennedy, C. Ling, E. Reynolds, M. Avdeev, A. Stampfl, Z. Zhang, L.-Y. Jang, Does local disorder occur in the pyrochlore zirconates? Inorg. Chem. 51 (2012) 13237-13244.

[8] C. Karthik, T. Anderson, D. Gout, R. Ubic, Transmission electron microscopic study of pyrochlore to defect-fluorite transition in rare-earth pyrohafnates. J. Solid State Chem. 194 (2012) 168-172.

[9] P. Blanchard, S. Liu, B. Kennedy, C. Ling, M. Avdeev, J. Aitken, B. Cowie, A. Tadich, Investigating the local structure of lanthanide hafnates $Ln_2Hf_2O_7$ via diffraction and spectroscopy. J. Phys. Chem. C 117 (2013) 2266-2273.

[10] J. Farmer, L. Boatner, B. Chakoumakos, M.-H. Du, M. Lance, C. Rawn, J. Bryan, Structural and crystal chemical properties of rare-earth titanate pyrochlores., J. Alloys Compd. 605 (2014) 63-70.

[11] V.V. Popov, A.P. Menushenkov, A.A. Yaroslavtsev, Ya.V. Zubavichus, B.R. Gaynanov, A.A. Yastrebtsev, D.S. Leshchev, R.V. Chernikov, Fluorite-pyrochlore phase transition in nanostructured $Ln_2Hf_2O_7$ (Ln = La-Lu). Journal of Alloys and Compounds 689 (2016) 669-679.

[12] J. Gardner, M. Gingras, J. Greedan, Magnetic pyrochlore oxides. Rev. Mod. Phys. 82 (2010) 53-107.

[13] W. Pan, S. Phillpot, C. Wan, A. Chernatynskiy, Z. Qu, Low thermal conductivity oxides. MRS Bull. 32 (2012) 917-922.

[14]. Levi CG. Emerging materials and processes for thermal barrier systems. Curr Opin Solid State Mat Sci. 8 (2004) 77–91.

[15]. Wan C, Qu Z, Du A, Pan W. Order-disorder transition and unconventional thermal conductivities of the $(Sm_{1-x}Yb_x)_2Zr_2O_7$ series. J Am Ceram Soc. 94 (2011) 592–596.

[16] V. Risovany, A. Zakharov, E. Muraleva, V. Kosenkov, R. Latypov, Dysprosium hafnate as absorbing material for control rods. J. Nucl. Mater 335 (2006) 163-170.

[17] R. Ewing, W. Weber, J. Lian, Nuclear waste disposal - pyrochlore ($A_2B_2O_7$): nuclear waste form for the immobilization of plutonium and ”minor” actinides. J. Appl. Phys. 95 (2004), 5949-5071.

[18] Kale, G.M., O’Carroll, D.P., Mudenda, S., Pang, W.K., Peterson, V.K., Rahayu, S., Forrester, J.S., Probing structural immiscibility in isometric pyrochlore oxide solid-solutions. J. Alloys and Comps, (in preparation, 2020).

[19] A.V. Shlyakhtina, S.N. Savvin, A.V. Levchenko, A.V. Knotko, Petra Fedtke, Andreas Busch, Torsten Barfels, Marion Wienecke,L.G. Shcherbakova. Study of bulk and grain-boundary conductivity of $Ln_{2+x}Hf_{2-x}O_{7-\delta}$ (Ln= Sm-Gd; x=0, 0.096) pyrochlores. J of Electroceramics. 24 (2010) 300-307.

[20] A.V. Shlyakhtina, N.V. Lyskov, A.N. Shchegolikhin, S.A. Chernyak, A.V. Knotko, I.V. Kolbanev, L.G. Shcherbakova. Structure evolution, ionic and proton conductivity of solid solutions based on $Nd_2Hf_2O_7$. Ceram. Intern. 46:11 (2020) 17383-17391. doi.org/10.1016/j.ceramint.2020.04.029.

[21] F.A. Lopez-Cota, N.M. Cepeda-Sanchez, J.A. Diaz-Guillen, O. J. Dura, O.M.A. Lopez, M. Maczka, M. Ptak, A. F. Fuentes, Electrical and thermophysical properties of mechanochemically obtained lanthanide hafnates. J Am Ceram Soc. 100 (2017) 1994-2004.

[22] P. Shojan, Y.S. Pavunny, K. Sudheendran, D. Sita, K. K. Rajesh, F.S. James, S.K. Ram, Holmium hafnate: An emerging electronic device material. Applied Physics Letters. 106 (2015) 112902.

[23] B.P. Mandal, N. Garg, S.M. Sharma, A.K. Tyagi, Preparation, XRD, and Raman spectroscopic studies on new compounds $RE_2Hf_2O_7$ (RE = Dy, Ho, Er, Tm, Lu,Y): pyrochlores or defect-fluorite?. J Solid State Chem. 179 (2006) 1990–94.

[24] Z. Wang, G. M. Kale, M. Ghadiri, Synthesis and characterization of $Ce_xGd_{1-x}O_{2-d}$ nanopowders employing an alginate mediated ion-exchange process. Chem. Eng. J. 198 (2012a) 149–153.

[25] Z. Wang, G. M. Kale, M. Ghadiri, Novel ion-exchange process for the reparation of metal oxide nanopowders from sodium alginate. J. Am. Ceram. Soc. 95 (2012b) 3124–3129.

[26] Z. Schnepp, S.C. Wimbush, S. Manna, S.R. Hall, Alginate-mediated routes to the selective synthesis of complex metal oxide nanostructures. Cryst. Eng. Comm. 12 (2010) 1410–1415, https://doi.org/10.1039/b923543b.

[27] S. Sardar, G.M. Kale, O. Cespedes, M. Ghadiri, Environmentally Sustainable Facile Synthesis of Nanocrystalline Holmium Hafnate ($Ho_2Hf_2O_7$): Promising New Oxide-ion Conducting Solid Electrolyte. SN Appl. Sci. 2:541 (2020). https://doi.org/10.1007/s42452-020-2336-9

[28] S. Sardar, G.M. Kale, M. Ghadiri, O. Cespedes, Structural Study of Holmium Zirconate Nanoparticles obtained through Carbon Neutral Sol Gel Process. Thermochimica Acta. 676 (2019) 120-129.

[29] S. Sardar, G.M. Kale, M. Ghadiri, Influence of processing conditions on the ionic conductivity of holmium zirconate ($Ho_2Zr_2O_7$). Ceramics International. 46 (2020) 11508-11514. https://doi.org/10.1016/j.ceramint.2020.01.177

[30] A. S. Mehranjani, D. J. Cumming, D. C. Sinclair, R. H. Rothman, Low-temperature co-sintering for fabrication of zirconia/ceria bi-layer electrolyte via tape casting using a Fe_2O_3 sintering aid, Journal of the European Ceramic Society. 37 (2017) 3981–3993.

[31] I. W. Chen, X.-H. Wang, Sintering dense nanocrystalline ceramics without final-stage grain growth, Nature. 404 (2000) 168-171.

[32] P. P. Edwards, V.L. Kuznetsov, W.I.F. David, N.P. Brandon, Hydrogen and fuel cells: Towards a sustainable energy future. Energy Policy 36 (2008) 4356–4362.

[33] D. R. Rittman, K. M. Turner, S. Park, A. F. Fuentes, C. Park3, R. C. Ewing, W. L. Mao, Strain engineered pyrochlore at high pressure, Nature Scientific Reports, 7 (2016) 2236-2237. https://doi.org/10.1038/s41598-017-02637-9

[34] H.M. Rietveld, A Profile Refinement Method for Nuclear and Magnetic Structures, J. Appl. Crystallogr. 2 (1969) 65–71.

[35] R.A. Young, 1993. The Rietveld Method, Oxford University Press Inc., New York.

[36] M. Adamu, G. M. Kale, Novel Sol−Gel Synthesis of $MgZr_4P_6O_{24}$ Composite Solid Electrolyte and Newer Insight into the Mg^{2+} Ion Conducting Properties Using Impedance Spectroscopy. J. Phys. Chem. C 120 (2016) 17909−17915.

[37] S.M. Haile, G. Staneff, K.H. Ryu, Non-stoichiometry, grain boundary transport and chemical stability of proton conducting perovskites. J Mater Sci. 36:5 (2001) 1149–1160.

[38] J.T.S. Irvine, D.C. Sinclair, A. R. West, Electroceramics: Characterization by Impedance Spectroscopy. Adv. Mater. 2:3 (1990)132-138.

[39] M.P. van Dijk, A.J. Burggraaf, A.N. Cormack, C.R.A. Catlow, Defect structures and migration mechanisms in oxide pyrochlores. Solid State Ionics. 17 (1985) 159–167.

[40] P.J. Wilde, C.R.A. Catlow, Defects and diffusion in pyrochlore structured oxides. Solid State Ionics. 112 (1998) 173–183.